



HAL
open science

Ultraviolet–visible–near-infrared optical properties of amyloid fibrils shed light on amyloidogenesis

Jonathan Pansieri, Véronique Josserand, Sun-Jae Lee, Anäelle Rongier, Daniel Imbert, Marcelle Moulin Sallanon, Enikö Kövari, Thomas Dane, Charlotte Vendrely, Odette Chaix-Pluchery, et al.

► **To cite this version:**

Jonathan Pansieri, Véronique Josserand, Sun-Jae Lee, Anäelle Rongier, Daniel Imbert, et al.. Ultraviolet–visible–near-infrared optical properties of amyloid fibrils shed light on amyloidogenesis. Nature Photonics, 2019, 13 (7), pp.473-479. 10.1038/s41566-019-0422-6 . hal-02181640

HAL Id: hal-02181640

<https://hal.science/hal-02181640>

Submitted on 24 Oct 2022

HAL is a multi-disciplinary open access archive for the deposit and dissemination of scientific research documents, whether they are published or not. The documents may come from teaching and research institutions in France or abroad, or from public or private research centers.

L'archive ouverte pluridisciplinaire **HAL**, est destinée au dépôt et à la diffusion de documents scientifiques de niveau recherche, publiés ou non, émanant des établissements d'enseignement et de recherche français ou étrangers, des laboratoires publics ou privés.

Ultraviolet-visible-near-infrared optical properties of amyloid fibrils shed light on amyloidogenesis

Jonathan Pansieri^{1,¶}, Véronique Josserand², Sun-Jae Lee^{1,3}, Anaëlle Rongier^{1,3}, Daniel Imbert³, Marcelle Moulin Sallanon^{4,5}, Enikő Kövari⁶, Thomas Dane⁷, Charlotte Vendrely^{8,9}, Odette Chaix-Pluchery⁹, Mélanie Guidetti², Julien Vollaire², Arnold Fertin¹⁰, Yves Usson¹⁰, Patrice Rannou³, Jean Luc Coll², Christel Marquette¹, Vincent Forge^{1,*}

¹ Univ. Grenoble Alpes, CEA, CNRS, BIG-LCBM, 38000 Grenoble, France

² Institute for Advanced Biosciences, Univ. of Grenoble Alpes - INSERM U1209 - CNRS UMR5309; F-38000 Grenoble, France

³ Univ. Grenoble Alpes, CEA, CNRS, INAC-SyMMES, 38000 Grenoble, France

⁴ INSERM U1039, La Tronche, F-38700, France

⁵ Univ. Grenoble-Alpes, Grenoble, F-38041, France

⁶ Department of Mental Health and Psychiatry, University Hospitals and University of Geneva School of Medicine, 2, chemin du Petit-Bel-Air, 1225 Geneva, Switzerland

⁷ European Synchrotron Radiation Facility, 71 avenue des Martyrs, B.P. 220, F-38043 Grenoble Cedex 9, France

⁸ Université de Cergy-Pontoise, I-MAT FD4122, ERRMECe, 95000 Cergy-Pontoise, France

⁹ Univ. Grenoble Alpes, CNRS, Grenoble INP, LMGP, 38000 Grenoble, France

¹⁰ CNRS, FR CNRS 3425; TMC-IMAG, F-38000 Grenoble, France

[¶] *Present address:* Department of Medical Biochemistry and Biophysics, Umeå University, 90187, Umeå, Sweden

**Corresponding author:* vincent.forge@cea.fr

Abstract: Amyloid fibres attract considerable interests due to their biological roles in neurodegenerative diseases and their potentials as functional biomaterials. We describe here a completely new finding about an intrinsic signal of amyloid fibres in the near infrared (NIR) range. When combined with their recently reported blue luminescence, it paves the way toward new blueprints for label-free detections of amyloid deposits within *in vitro* up to *in vivo* contexts. The blue luminescence allows for staining-free characterization of amyloid deposits within human samples. The NIR signal offers promising prospects for innovative diagnostic strategies of neurodegenerative diseases; a need to improve medical care and to develop new therapies. As a proof of concept, we demonstrate direct detection of amyloid deposits within brains of living aged “Alzheimer’s” mice using non-invasive and contrast agent-free imaging. UV-Vis-NIR optical properties of amyloids opens new research avenues across amyloidoses as well as for next generation biophotonic devices.

Amyloid fibres result from the self-assembly of polypeptides into high-aspect ratio nanowires¹⁻³. These supramolecular protein assemblies are studied for their biological roles^{1,2} and for their potential as new biomaterials⁴⁻⁶. They have been widely studied within the context of neurodegenerative diseases, such as Alzheimer's and Parkinson's diseases, because they are the constituents of amyloid deposits, a hallmark of these disorders^{7,8}. Note that amyloid deposits are also found within several tissues in relation to diseases such as type 2 diabetes and systemic amyloidosis⁹. To date, 36 amyloid fibre proteins have been identified in Humans. As disease-related structures, a special attention is given to their formation mechanisms with the ultimate aim to understand their relationships with disorder developments^{10,11}. It is indeed of paramount importance to decipher the key steps at the origin of their formation and accumulation into amyloid deposits, and to characterize the toxic species and their generation¹¹. Another equally important research axis concerns the detection of amyloid deposits for the *in vivo* diagnosis of amyloidoses. Indeed, in the case of Alzheimer's and Parkinson's diseases, for instance, a diagnosis is needed not only for a better medical care but also for the development of new therapies^{12,13}. Nowadays, the diagnosis is based on the detection of mild cognitive impairment, which is not without ambiguity. As a consequence, biomarkers are sought to complete the diagnosis and targeting the amyloid deposits seems to be promising for that purpose.

We describe here generic UV-Vis-NIR optical properties of amyloid fibres, drawn from the characterization of amyloid fibres made of 13 proteins either involved in diseases or not (Table 1). Beside the blue luminescence which has been already described *in vitro* for amyloid fibres, other protein aggregates and within metabolite amyloid-like structures¹⁴⁻²¹, we report a near infrared (NIR) signal specific of the amyloid fibre structure. Although the underlying basic phenomena at their origin remain mostly unknown to date, these optical properties are of considerable potential interests for the investigation (both *in vitro* and *in*

vivo) of the amyloid-based disease development. The two types of optical signal allow not only label-free kinetic studies of the fibre self-assembly mechanisms but also the monitoring of different key steps. The blue luminescence allows to characterize amyloid deposits within biological samples (mice and human) and to characterize their morphology within biological environment without the need for specific staining procedures. Ultimately, the NIR signal is of interest. We demonstrate that it allows for the detection of amyloid deposits within the brain of living rodents using *in vivo* non-invasive real time and contrast agent-free imaging through the skull of mice. Its importance for human amyloidosis applications needs to be further researched.

UV-Vis-NIR properties of amyloid fibres

The fascinating luminescent properties of amyloid fibres spanning across the visible up to the near infrared (NIR) part of the spectrum are illustrated *in vitro* with the prion-domain of Het-s on an amyloid fibres suspension (Fig. 1a) and by fluorescence microscopy onto highly oriented amyloid fibres within a micro wire (Fig. 1b) resulting from the self-organization of a drop drying in between two tips (Supplementary Fig. 1). Depending on the excitation wavelength, the microwire appears with colours ranging from blue (with an excitation in the near-UV) up to red-near infrared (Fig. 1b). These observations performed on dry aligned fibres can be related to spectroscopic measurements on a suspension of amyloid fibres made of the Het-s prion-domain (Fig. 1a). Upon near-UV excitation, a blue luminescence is first detected. The emission peak is quite broad and its maximum experiences a bathochromic shift with the excitation of increasing wavelength. Luminescent properties can also be observed in the red-NIR range; the emission maximum depending drastically on the excitation wavelength. The intensity of the NIR signal is found to be *ca.* 30 times lower than the one of the blue luminescence; the exact ratio depending on the protein concentration.

Similar observations can be made with amyloid fibres made of A β ₁₋₄₂, both *in vitro* and within a biological context (Fig. 1c&d). *In vitro*, the optical properties of an A β ₁₋₄₂ amyloid fibre suspension (Fig. 1c) are similar to those described above. *In vivo*, A β ₁₋₄₂ forms amyloid deposits within the brain of aged “Alzheimer’s Disease” (AD) mice (18 months)^{22,23}, overexpressing human A β ₁₋₄₂, that can be detected *ex vivo* within the cortex area of these AD mice upon Thioflavin S labelling (Supplementary Fig. 2). These amyloid deposits can be detected without staining by fluorescence microscopy (Fig. 1d) using parameters identical to those used above for the aligned amyloid fibres. Note importantly that nothing noticeable can be seen in transmission. These stains are not seen on brain section of middle age control mice (Supplementary Fig. 3). Two different patterns can be distinguished: sharp spots and much broader stains with a denser centre and a more diffuse periphery (Fig. 1d). Only the last pattern is typical of amyloid deposits^{22,23}. The sharper spots are barely detectable in the blue range (Fig. 1d) suggesting that they are not made of amyloid deposits. We tentatively linked them to lipofuscins, granules of lipids and pigments with a strong auto-fluorescence^{20,24,25}, which are known to accumulate with age within several organs^{26,27}, as observed in control aged mouse brain (Supplementary Fig. 4), showing that their presence is not univocally related to Alzheimer’s disease^{28,29}.

Blue luminescence *in vitro* and within human samples

In agreement with previous studies¹⁴⁻¹⁷, the blue luminescence is observed for all amyloid fibres investigated in this study (Table 1). This luminescent behaviour is illustrated with representative proteins (Fig. 2 and Supplementary Fig. 5) as well as for proteins involved in diseases (Fig. 1c and Supplementary Fig. 6). Although the luminescent behaviour is not identical for every amyloid fibre (Table 1), generic characteristics can be determined (see the Supplementary section). The emission maxima are invariably located within the 430-450 nm

spectral range and are dependent on the excitation wavelength for most fibres. A weak blue luminescence is usually detected for the monomeric polypeptides (Fig. 2 and Supplementary Fig. 5). However, a significant enhancement of the intensity is observed upon fibre formation (Table 1). The excitation spectra are remarkably similar with a band centred at *ca.* 350-370 nm (Fig. 2a and Supplementary Fig. 5). When possible, estimations of the molar extinction (ϵ) for this transition give values of *ca.* 300-450 M⁻¹.cm⁻¹ (Table 1 and Supplementary Fig. 5). The luminescence quantum yield is rather low³⁰ (*ca.* 0.01) with typical lifetimes of *ca.* 1-3 ns.^{14,16,17} Several tentative explanations have been proposed for this luminescence, such as the occurrence of quantum confinement due to the sub-10 nm size of the supramolecular assemblies^{18,31} or charge delocalization within the H-bond network stabilizing the fibres²⁴. A similar blue luminescence, nicknamed “non-traditional intrinsic luminescence” (NTIL), has been reported for supramolecular architectures lacking traditional luminophores, including amyloid fibres. This luminescence is related to the aggregation/confinement of electron-rich hetero-atomic moieties³³.

Strikingly, the blue luminescence we observed is intense enough to allow the monitoring of the structure of amyloid deposits by confocal microscopy within a human brain section from an Alzheimer’s patient. The Figure 3 shows 3D reconstructions of two amyloid deposits with different structures; typical sections are shown within the insets. The first one (Fig. 3a) is a dense packing and fibrillary structures that can be distinguished on the periphery only, while the second one (Fig. 3b) is a fibre embedding with a more homogenous distribution of fibres. This allows also a sight on their surroundings. The first one is surrounded by brain tissues and looks like a pompon associated to a blood vessel (Fig. 3a); very similar to deposits observed within AD brains, either human³⁴ or mice³⁵. The second one seems more isolated (Fig. 3b). Movies showing the internal structures and (movies M1 & M2)

the 3D external envelopes (movies M3 & M4) of both amyloid deposits have been built from the sequential confocal images.

***In vitro* NIR signal**

The NIR signal is unequivocally linked to the supramolecular structure of the amyloid fibres (Supplementary Fig. 1) since no signal is recorded in the case of monomeric proteins (Fig. 2 and Supplementary Fig. 5). Within the wavelength range investigated in this study, the maximum of the NIR signal continuously shift with a linear dependency between the excitation and the maximum emission wavelengths (Supplementary Fig. 7), indicating a constant Stokes shift of *ca.* 55-60 nm (Table 1). The origins of this luminescence, which is also present within amyloid fibres without aromatic side-chains (Supplementary Fig.5), remain to be understood. This NIR signal has the following two remarkable features: *i*) it is detectable on a very broad wavelength range with a constant Stokes shift and *ii*) it has a rather narrow emission, narrowing further as the width of the emission monochromator slit width decreases (Supplementary Fig. 8), suggesting that the NIR signal is due to an inelastic light scattering rather than from a relaxation of excited states within the fibres. This tentative explanation is further supported by the impossibility to determine lifetimes for the NIR signal (value lower than 0.1 ns), while expected values of lifetimes for singlet and triplet excited states (*ca.* 1 ns vs. *ca.* 100 μ s) could be measured for Lysozyme amyloid fibres (not shown). In addition, the Stokes shift is around 1200-1400 cm^{-1} (Supplementary Fig. 8), in good agreement with the Raman shift of the amide I-III bands of proteins³⁶. Moreover, the appearance of the NIR signal seems correlated with an enhancement of the Raman signal due to the organization of the proteins within amyloid fibres³⁷ (Supplementary Fig.9). Similarly to the blue photoluminescence, the NIR signal intensity increases regularly with the protein concentration without aggregation-induced quenching (Supplementary Fig. 10). Altogether,

these observations point toward an enhancement of the Raman signal, due to protein self-assembly into highly organized amyloid fibres³⁷ as the tentative explanation of the NIR signal. Till date, only a preliminary correspondence between the position of the NIR signal and the Raman spectrum (several bands between 1000 cm^{-1} and 1700 cm^{-1}) is observed. Unexpectedly for a Raman spectrum, the position of the NIR signal shifts with the excitation wavelength: from 1400 cm^{-1} to 1160 cm^{-1} within the wavelength range investigated (Supplementary Fig. 8). This effect might be due to the fact that i) these experiments were performed with a spectrofluorimeter where the excitation is not monochromatic but had a finite bandwidth (slits), on the contrary to a Raman spectrometer which uses a monochromatic laser light, and ii) the NIR signal excitation seems to have a maximum (Fig. 2). When the excitation wavelength increases and moves away from its optimal value (as it is the case in Supplementary Fig. 8), the contribution of high energy photons to the emitted light will increase compared to that of lower energy ones. This will result in an apparent decrease of the energy difference between the excitation spectrum and the emission spectra, *i.e.* an apparent decrease of the Stokes shift as the excitation wavelength increases. Anyway, the correspondence between our NIR signal and Raman scattering is not unambiguously established; other possibilities such as optical effects due to the size (hundreds of nanometers) and shape (high aspect ratio) of amyloid fibres remaining to be evaluated.

Monitoring kinetics of fibril formation without external probe

The investigation of the amyloid fibre formation is of prime importance to unravel the molecular events at the origin of the disease development. To date, a fluorescent marker must be used to monitor fibres formation, the most commonly used being Thioflavin T (ThT)^{10,11}. However, several assumptions lie behind its use³⁸, concerning i) ThT effect on the amyloid fibril formation kinetics and ii) the proportionality between ThT signal and the amount of

amyloid fibres. The blue luminescence and NIR signal should be valuable intrinsic probes of the fibre formation. The possibility of using the blue luminescence has been already demonstrated¹⁷. However, it remains ambiguous due to the fact the blue luminescence has been reported for other protein aggregates than amyloid fibres, such as crystals for instance^{19,33}. The NIR signal, which is observed only upon formation of amyloid fibres, holds potential for becoming a truly unambiguous probe. The NIR signal and the blue luminescence are proportional to the protein concentration (Supplementary Fig. 11), when A β ₁₋₄₂ fibres are depolymerized by adding HFIP, the NIR signal vanishes (Supplementary Fig. 11). For a first proof of concept demonstration, the amyloid fibre formation of insulin has been simultaneously monitored by the blue and NIR signal changes (Fig. 2c). Obviously, the blue luminescence begins to appear before the NIR signal as seen after 2 hours (Fig. 2c and Supplementary Fig. 12). This suggests that the phenomenon at the origin of the blue luminescence precedes the fibre growth, likely because of early intermediates. In a separate experiment we have checked that NIR signal superimpose with the ThT fluorescence build up (Supplementary Fig. 13).

In vivo* NIR signal: imaging of amyloid deposits *in vivo

The intrinsic NIR signal of amyloid fibres is of particular interest as it falls within the so-called “diagnostic windows”. NIR photons are attractive for non-invasive analyses as they can cross significant depths of biological tissues, opening doors toward non-invasive imaging for monitoring biological functions/dysfunctions within live tissues longitudinally over time^{39,40}. Due to its particular nature, it was impossible to measure a quantum yield for the NIR signal. In order to estimate its intensity, we made a comparison with Cyanine 5.5, a fluorophore used for *in vivo* NIR imaging and of known quantum yield⁴¹ (Supplementary Fig. 14). After normalization of the concentrations, the NIR signal of amyloid fibres appeared to

be around three orders of magnitude weaker than that of Cyanine 5,5. However, this low signal could be compensated *in vivo* due to the high density of amyloid deposits. Indeed, the *in vitro* NIR signal increases regularly with the protein concentration, *i.e.* without aggregation-induced quenching (Supplementary Fig. 10), and signal intensity of a dried droplet is high (Supplementary Fig. 14).

The use of continuous-wave NIR fluorescence-enhanced diffuse optical tomography (fDOT) allows for a fast, 3D and quantitative measurement of the NIR signal distribution in the scanned volume of interest at each time point. The disease progression can thus be precisely and accurately monitored in a given animal overtime^{42,43}. fDOT imaging ($\lambda_{\text{exc.}} = 690$ nm and $\lambda_{\text{em.}} = 730 \pm 30$ nm) has been performed on eleven advanced age AD mice together with eleven control wild type mice (Fig. 4). Live animal imaging was performed non-invasively and without the use of any contrast agent. Both populations had similar age distributions (18.4 ± 2.6 months for both groups) (Fig. 4d). Figures 4a&b (top panels) show typical 3D brain images (total integrated signal) of AD and control mice. Overall, the NIR signal was 6 times more intense in the AD mice (Fig. 4c) as compared to controls ($p < 0.05$, Student T-test). Fresh brain sections from these same mice were then observed by epifluorescence in the visible wavelength range using a MacroFluo fluorescence stereomicroscope. Typical granular structures could be observed within the cortex area of AD mice while those of control mice appeared completely devoid of particular patterns (Figs. 4a-b, bottom panels), indicating that the fDOT intensity increase was related to the accumulation of amyloid deposits. The excitation wavelength used for these fDOT experiments: 690 nm, together with that of the following 2D NIR imaging: 780 nm, were far beyond the beyond the maximum of the lipofuscin's emission spectrum: 600-650 nm.^{20,30} Therefore it is very unlikely that the NIR signal increase was due to lipofuscin. This illustrates an advantage of the amyloid NIR signal.

It occurs on an extremely broad wavelength range (Supplementary Fig. 8) and importantly enables to distinguish amyloid fibres from other possible sources of luminescence.

The increased *in vivo* NIR signal measured using fDOT could also be seen using non-invasive 2D NIR imaging (Fluobeam[®]800)⁴⁴ on the head of living mice under anaesthesia (Fig. 5a-b, top panels) as well as on extracted whole brains after mice sacrifice (Fig. 5a-b, bottom panels). We then hypothesized that the NIR signal-contrasted granular structures seen on the MacroFluo images (Fig. 4) should also be registered by the Fluobeam[®]800 although the presence of heterogeneities was not distinguishable by naked eyes on the images. This indeed arose by mapping the NIR signal intensity distribution within the image in a 3D graph (Fig. 5c). By that means, AD mice were shown to display both higher NIR signal intensities and increased speckles as compared to those from the control group. The variation of intensity of each pixel was compared to its closest neighbours (Mean Local Standard Deviation, MLSD), or as a function of the slopes of variations (Mean Gradient, MG), on brain regions of interest (see methods). These methods of analysis allowed to demonstrate that we could detect speckles due to pixel to pixel heterogeneities more often in the AD mice group than in the WT group, both in images taken non-invasively in living animals (Fig. 5d, top panels) and *ex vivo* in whole brains extracted after sacrifice (Fig. 5d, bottom panels). Thus, by using MLSD and MG, two populations stood out and AD mice could be distinguished from the control mice (Fig. 5e) with only two exceptions (one in each panel, either “AD” or “control”). In particular, one AD mouse displayed several dark skin marks that definitely interfered in NIR signal evaluation and led to misattribution.

Conclusions

In summary, we describe two optical signatures of amyloid fibres: a luminescence in the blue and a NIR signal, which can be observed *in vitro* and *in vivo* on tissues. These features allow for the direct detection of amyloid structures without labelling. *In vitro*, this is of particular interest to monitor the fibrillation kinetics without the need of an extrinsic probe which can possibly interfere with the reaction. Moreover, it seems that the two types of signatures reflect different phenomena involved in the self-assembly mechanism. Furthermore, such detection and quantification could allow also investigations on *ex-vivo* thick tissue sections without staining procedures. The NIR signal holds particular interests for *in vivo* detection of amyloid deposits that should be further investigated in the human brain³⁹, and also in other organs where amyloidosis is involved. This could establish this amyloid-specific NIR signal as new blueprints for the study of amyloidoses. We indeed show that aged Alzheimer's mice model has a stronger and more heterogeneous NIR signal that can be detected by 3D imaging in the NIR domain but also using non-invasive and real time 2D NIR imaging on alive animals. In case the NIR signal would correspond to an enhancement of spontaneous Raman scattering, this would hold high interest not only to detect but also to characterize *in situ* amyloid deposits, in particular via stimulated Raman scattering approaches^{45,46}. Moreover, as amyloid fibres attract considerable interests for the design of functional bio-nanomaterials, taking advantages of the peculiar optical properties of amyloid fibres described here can be envisioned⁴⁷⁻⁴⁹. This is extending the scope of the presented results well beyond the ones of neurodegenerative diseases by opening doors to bioinspired photonic devices exploiting the vastly unexplored to date visible to NIR luminescent properties of protein self-assembled into amyloid fibres.

Methods

Fibril growth: The Amyloid fibres of the Het-s prion domain were obtained as previously described³. The A β ₁₋₄₂, IAPP and TTR(V30M) fibres were formed as previously described⁵⁰. CSNNFGA peptide (Genecust) is a derived-sequence from IAPP, so CSNNFGA fibres were formed following the same protocol as IAPP fibres. The hTau and α -synuclein fibres were formed as previously described⁵¹. Lyophilized lysozyme (Sigma-Aldrich, L-6876) and human serum albumin (Sigma-Aldrich, A-3732) were directly dissolved in a 50mM glycine, 88mM NaCl buffer and adjusted to pH 2.7 to obtain respectively a final concentration at 1mM and at 250 μ M, incubated at 65°C during 3 days. For lysozyme fibrillation, a rotating shaker (500 rpm) was used⁵². Insulin fibres were formed using lyophilized insulin (Sigma-Aldrich, I6634-1G) in a 20% acetic acid buffer, adjusted at pH 1.7 at 40°C on a rotating shaker (500 rpm) during 10 hours. Lyophilized β -lactoglobulin (Sigma-Aldrich, L3908-5G) was dissolved in deionized water (2mM) adjusted at pH 2 and 335 K, filtered through a 0.22 μ m before 10 days of incubation, adapted from published protocols⁵³. The α -lactalbumin (Sigma-Aldrich, L6010-1G) fibres were obtained as previously described³. The NNLAIVTA (Proteogenix) fibres have been formed in a Hepes 10mM buffer at a final concentration at 1.5mM at pH 7.4⁵⁴. All fibres morphologies were confirmed using Transmission Electronic Microscopy (TEM) analysis (performed on a Tecnai 12 microscope).

Fluorescence spectroscopy: Measurements on amyloid proteins were carried out on a JASCO FP-8500 and a Fluorolog FL3-22 spectrophotometers from Horiba-Jobin Yvon-Spex (equipped with a double grating excitation monochromator and an iHR320 imaging spectrometer). Each spectrum was recorded in a 1 cm path length quartz cell, with a response time of 1 sec, an excitation bandwidth of 5 nm and an emission bandwidth of 10 nm. Excitation spectra of lysozyme, insulin and NNLAIVTA fibres were recorded at the maximum of the emission peak for each emission spectra, with same parameters. Kinetic studies of insulin fibre formation were carried out using 200 μ M of Insulin with freshly

dissolved Thioflavin T at 30 μ M during 5 and 30 hours, with the same parameters, UV-Vis and NIR emission spectra under respective excitation at 360 nm and at 640 nm, and the emission spectra of ThT with an excitation at 440 nm (and an emission peak around 485nm). Absorption spectra recorded using a JASCO J-815 CD-spectrophotometer, using a 1 cm path length quartz cell, with a response time of 1 sec, a bandwidth of 4 nm, each 1 nm between 190 and 700 nm.

For lifetime measurements, excitation of the amyloid fibers was accomplished by a i) a nanoled source with a laser diode head N-375L (FWHM < 10 nm, pulse < 88 ps), ii) a nanoled source with a laser diode head N-650L (FWHM < 10 nm, pulse < 70 ps) or iii) a nanoled source with a led head N-740 (FWHM 20 nm, pulse < 800 ps) from Horiba Scientific. The nanoleds were coupled to a Jobin Yvon NL-C2 Pulse Diode controller and a DH-HT TCSPC controller allowing the measurement of fluorescence lifetimes < 100 ps and relied to the Fluorolog FL3-22 spectrometer from Horiba-Jobin Yvon-Spex. The output signal of the photomultiplier was fed to a PC and controlled and analyzed with the Data Station (v2.7) and Decay Analysis (v6.8) software from Horiba Scientific. Lifetimes are averages of 3 independent determinations with a calculated Chi-square < 2.

Raman microspectroscopy: Raman spectra were recorded using a Jobin Yvon/Horiba LabRam spectrometer equipped with a liquid nitrogen cooled charge-coupled device detector. The experiments were conducted in the micro-Raman mode at room temperature in a backscattering geometry. The 632.8 nm line from a He-Ne laser was focused to a 1 μ m² spot on the sample surface using a x50 long working distance objective with an incident laser power close to 5.3 mW. Raman spectra were calibrated using a silicon reference spectrum at room temperature.

WAXS: Aligned amyloid fibres made of the Het-s prion domain were obtained by drying a highly concentrated fibre suspension between two tips. The X-Ray diffraction pattern was

recorded at ESRF (Grenoble) on the microfocus beamline ID13 using a $2 \times 2 \mu\text{m}^2$ X-ray beam (energy $E = 13 \text{ keV}$, wavelength $\lambda = 0.9537 \text{ \AA}$).

Alzheimer's mice brain sections: Brain sections of APP^{swE}/PSEN1^{dE9} mice model (kindly provided by B. Larrat, Saclay, France) with Alzheimer's disease (aged 18 months) were mounted on slice without labelling. As control, brain sections from C57/Bl6 mice were used (12 months old). Mice were deeply anesthetized with a mixture of xylazine/ketamine before sampling. Animals were intracardiacally perfused with PBS buffer, followed by PFA 4% fixative solution. Brains were removed from the skull and post-fixed for 24 hours at $4 \text{ }^\circ\text{C}$ in PFA 4% and afterward transferred in PBS buffer with 0.1% NaN_3 , before microtome sectioning ($20 \mu\text{m}$, Leica, VT 1000E) and conserved mounted on a glass-slide at -20°C . All the procedures involving animals were carried out in accordance with the European community council directives. Intrinsic fluorescence properties were recorded with a Zeiss microscope Axiovert 200 M, at various wavelength, with emission in blue ($\lambda_{\text{exc.}} = 390 \pm 10 \text{ nm}$, $\lambda_{\text{em.}} = 460 \pm 50 \text{ nm}$), green ($\lambda_{\text{exc.}} = 475 \pm 10 \text{ nm}$, $\lambda_{\text{em.}} = 530 \pm 50 \text{ nm}$), yellow ($\lambda_{\text{exc.}} = 545 \pm 25 \text{ nm}$, $\lambda_{\text{em.}} = 605 \pm 70 \text{ nm}$) and in NIR with false red colour ($\lambda_{\text{exc.}} = 620 \pm 60 \text{ nm}$, $\lambda_{\text{em.}} = 700 \pm 75 \text{ nm}$). Images were analysed with Carl Zeiss software and Image I 1.50 software.

Human samples: Brains were obtained by autopsies from the Department of Internal Medicine, Rehabilitation and Geriatrics, Division of Geriatrics, and the Department of Readaptation and Palliative Medicine, University Hospitals, Geneva with the approval from the Ethics Committee of the University of Geneva. We included two brain autopsies from a control and an Alzheimer's disease cases performed in 2015. For neuropathological analysis, tissues blocks were taken from the hippocampus with the inferior temporal cortex (Brodmann area 20). Brain tissue was fixed in buffered formaldehyde 4% for 4 weeks. From paraffin embedded blocs adjacent sections of $30\mu\text{m}$ -thick were realized and paraffin was removed using successive xylene / ethanol baths. Floating slices were finally conserved in phosphate

buffer saline (sodium azide 0.05%) until histological treatment. Intrinsic luminescence properties were recorded with Zeiss confocal LSM800 microscope, at various wavelength, in blue ($\lambda_{exc.}$: 350-420 nm, $\lambda_{em.}$: 440-500 nm), green ($\lambda_{exc.}$: 450-500 nm/ $\lambda_{em.}$: 480-550 nm), and NIR ($\lambda_{exc.}$: 620-700 nm/ $\lambda_{em.}$: 640-750 nm). Images were analysed with Carl Zeiss software, Vaa3D and Image I 1.50 software.

Immunohistochemistry: Frozen sections were processed for immunohistochemistry for amyloid burden staining with Thioflavin S ($\lambda_{exc.}$ = 450 nm – $\lambda_{em.}$ = 488 nm) (Sigma, #T1892) according to standard practice. Fluorescent images were obtained from either a Zeiss confocal LSM800 microscope or Zeiss microscope Axiovert 200 M for human sections and brain tissues, respectively. Images were analysed using Carl Zeiss Zen software and Image J 1.50f software.

In vivo and ex vivo imaging: All animal experiments were performed in accordance with the European Economic Community guidelines and the “Principles of Laboratory Animal Care” (NIH publication N 86-23 revised 1985). The protocols were approved by an animal ethics committee and received the authorization of the French Ministry of Higher Education and Research (authorization #8854-2017031314338357).

Female APP^{swe}/PSEN1^{dE9} and C57/Bl6 mice (n=11 per group) were bred until 18.4^{±0.7} months' old. The day before imaging, mice were anesthetized (isoflurane/air 4% for induction and 1.5% thereafter) and their heads were shaved. For non-invasive, continuous-wave NIR fluorescence-enhanced diffuse optical tomography (fDOT) NIR imaging, anesthetized mice were placed in a previously described prototype imaging system⁴². Briefly, mice heads were illuminated with a monochromatic 690 nm laser light. The irradiance on the imaging field is 14 mW/cm². The reemitted signal was filtered with a band pass 730AF30 filter (30 nm band cut centred at 730 nm), placed in front of a NIR-sensitive CCD camera (Hamamatsu ORCA AG) mounted with a f/15-mm objective (Schneider Kreuznach). All mice were scanned over

a 2 cm² rectangle surface on the head and a dedicated algorithm generated a 3D reconstruction of NIR signal distribution in the head mice⁴³. Total NIR signal within the reconstructed volume (arbitrary units) was quantified for all mice.

Mice were then imaged using the Fluobeam[®]800 (Fluoptics, France) ($\lambda_{exc.} = 780$ nm, $\lambda_{em.} > 820$ nm; 500 ms exposure time) directly on the live animals and after sacrifice and exposure of the entire brain. The irradiance on the imaging field is 10 mW/cm². Please note that for both imaging systems exposure times may vary from 100 ms to 10 s. These combinations of power and exposure times correspond to a maximum energy of 140 mJ/cm² which is far lower than the maximum permissible exposure limit for skin at these wavelengths (2 J/cm²). For each individual a ROI (Region Of Interest) was defined manually. Two analysis methods were used to quantify the grey level variations within each ROI. The first analysis corresponds to the local standard deviation between a given pixel and its neighbourhood delimited by a circular region of a given radius (here $r = 3$). For each individual, the average value of these standard deviations was calculated within the Mean Local Standard Deviation (MLSD). The second analysis corresponds to the mean gradient measurement (Mean Gradient, MG). The gradient is conventionally estimated by convolution with the partial derivatives of a Gaussian kernel parameterized with $\sigma = 1$.

For *ex vivo* fluorescence microscopy, mice were euthanized, brains were isolated, coronal slices were cut using a brain matrix (1.0 mm, Stoelting, USA) and mounted between slide and coverslip. Macroscopic fluorescence imaging was performed with a MacroFluo (Z16 APO, Leica, Germany) fluorescence stereomicroscope, equipped with a high-sensitive CCD camera (iKon-M, Andor, Northern Ireland) with a 515-560 nm excitation and a 590 nm long pass emission filter. Images were acquired with an objective x0.8 at x2.5 magnification.

REFERENCES:

1. Eisenberg, D. & Jucker, M. The amyloid state of proteins in human diseases. *Cell* **148**, 1188-1203 (2012).
2. Knowles, T.P., Vendruscolo, M. & Dobson, C. M. The amyloid state and its association with protein misfolding diseases. *Nat. Rev. Mol. Cell. Biol.* **15**, 384-396 (2014).
3. Doussineau, T. et al. Mass Determination of Entire Amyloid Fibers by Using Mass Spectrometry. *Angew. Chem. Int. Ed.* **55**, 2340-2344 (2016).
4. Knowles, T.P.J. & Mezzenga, R. Amyloid fibers as building blocks for natural and artificial functional materials. *Adv. Mater.* **28**, 6546-6561 (2016).
5. Aumüller T. & Fändrich M. Protein chemistry: catalytic amyloid fibers. *Nat. Chem.* **6**, 273-274 (2014).
6. Altamura, L. et al. A synthetic redox biofilm made from metalloprotein-prion domain chimera nanowires. *Nat. Chem.* **9**, 157-163 (2017).
7. Kovacs, G.G. Molecular Pathological Classification of Neurodegenerative Diseases: Turning towards Precision Medicine. *Int. J. Mol. Sci.* **17**, 189 (2016).
8. Jucker, M. & Walker, L.C. Self-propagation of pathogenic protein aggregates in neurodegenerative diseases. *Nature* **501**, 45-51 (2013).
9. Sipe, J.D. et al. Amyloid fibril proteins and amyloidosis: chemical identification and clinical classification International Society of Amyloidosis 2016 Nomenclature Guidelines. *Amyloid* **23**, 209-213 (2016).
10. Knowles T.P. et al. An analytical solution to the kinetics of breakable filament assembly. *Science* **326**, 1533-1537 (2009).
11. Glabe, C.G. Common mechanisms of amyloid oligomer pathogenesis in degenerative disease. *Neurobiol. Aging* **27**, 570–575 (2017).
12. Cummings, J.L., Doody, R. & Clark, C. Disease-modifying therapies for Alzheimer disease: challenges to early intervention. *Neurology* **69**, 1622-1634 (2007).
13. Stower, H. Searching for Alzheimer’s disease therapies. *Nat. Med.* **24**, 894-897 (2018).
14. Del Mercato, L. L. et al. Charge transport and intrinsic fluorescence in amyloid-like fibers. *Proc. Natl. Acad. Sci. U. S. A.* **104**, 18019-18024 (2007).
15. Tcherkasskaya, O. Photo-activity induced by amyloidogenesis. *Protein Sci.* **16**, 561-571 (2007).

16. Chan, F.T. et al. Protein amyloids develop an intrinsic fluorescence signature during aggregation. *Analyst* **138**, 2156-2162 (2013).
17. Pinotsi, D., Buell, A.K., Dobson, C.M., Kaminski Schierle, G.S. & Kaminski, C.F. A label-free, quantitative assay of amyloid fibril growth based on intrinsic fluorescence. *Chembiochem.* **14**, 846-850 (2013).
18. Handelman, A., Beker, P., Amdursky, N. & Rosenman, G. Physics and engineering of peptide supramolecular nanostructures. *Phys. Chem. Chem. Phys.* **14**, 6391-6408 (2012).
19. Shukla, A. et al. A novel UV laser-induced visible blue radiation from protein crystals and aggregates: scattering artifacts or fluorescence transitions of peptide electrons delocalized through hydrogen bonding? *Arch. of Bioch. and Bioph.* **428**, 144-153 (2004).
20. Zipfel, W.R. et al. Live tissue intrinsic emission microscopy using multiphoton-excited native fluorescence and second harmonic generation. *Proc. Natl. Acad. Sci. U. S. A.* **100**, 7075-7080 (2003).
21. Shaham-Niv, S. et al. Intrinsic Fluorescence of Metabolite Amyloids Allows Label-Free Monitoring of Their Formation and Dynamics in Live Cells. *Angew. Chem. Int. Ed.* **57**, 12444-12447 (2018).
22. Kuo, Y.M. et al. Comparative analysis of amyloid-beta chemical structure and amyloid plaque morphology of transgenic mouse and Alzheimer's disease brains. *J. Biol. Chem.* **276**, 12991-12998 (2001).
23. Matsuoka, Y. et al. Inflammatory responses to amyloidosis in a transgenic mouse model of Alzheimer's disease. *Am. J. Pathol.* **158**, 1345-1354 (2001).
24. Marmorstein, A. D., Marmorstein, L. Y., Sakaguchi, H., & Hollyfield, J. G. Spectral Profiling of Autofluorescence Associated with Lipofuscin, Bruch's Membrane, and Sub-RPE Deposits in Normal and AMD Eyes. *Invest. Ophthalmol. Vis. Sci.* **43**, 2435-2441 (2002).
25. Haralampus-Grynaviski, N. M. et al. Spectroscopic and morphological studies of human retinal lipofuscin granules. *Proc. Natl. Acad. Sci. U. S. A.* **100**, 3179-3184 (2003).
26. Youssef, S. A. et al. Pathology of the Aging Brain in Domestic and Laboratory Animals, and Animal Models of Human Neurodegenerative Diseases. *Veterinary Pathology* **53**, 327-348 (2016).
27. Gilissen, E. P. et al. A neuronal aging pattern unique to humans and common chimpanzees. *Brain Struct. Funct.* **221**, 647-664 (2016).

28. Dowson, J. H., Mountjoy, C. Q., Cairns, M. R., Wilton-Cox, H. & Bondareff, W. Lipopigment Changes in Purkinje Cells in Alzheimer's Disease. *J. Alzheimer's Disease* **1**, 71–79 (1998).
29. D'Andrea, M. R. et al. Lipofuscin and Ab42 exhibit distinct distribution patterns in normal and Alzheimer's disease brains. *Neuroscience Lett.* **323**, 45–49 (2002).
30. Niyangoda, C., Miti, T., Breydo, L., Uversky, V. & Muschol, M. Carbonyl-based blue autofluorescence of proteins and amino acids. *PLOS ONE* **12**, e176983 (2017).
31. Tao, K. et al. Quantum confined peptide assemblies with tunable visible to near-infrared spectral range. *Nat. Commun.* **9**, 3217 (2018).
32. Pinotsi, D. et al. Proton Transfer and Structure-Specific Fluorescence in Hydrogen Bond-Rich Protein Structures. *J. Am. Chem. Soc.* **138**, 3046-3057 (2016).
33. Tomalia, D. A. et al. Non-traditional intrinsic luminescence: inexplicable blue fluorescence observed for dendrimers, macromolecules and small molecular structures lacking traditional/conventional luminophores. *Prog. Polym. Sci.*, (2018) DOI: 10.1016/j.progpolymsci.2018.09.004
34. Plascencia-Villa, G. et al. High-resolution analytical imaging and electron holography of magnetite particles in amyloid cores of Alzheimer's disease. *Sci. Rep.* **6**, 24873 (2016).
35. Meyer, E.P., Ulmann-Schuler, A., Staufenbiel, M. & Krucker, T. Altered morphology and 3D architecture of brain vasculature in a mouse model for Alzheimer's disease. *Proc. Natl. Acad. Sci. U. S. A.* **105**, 3587-3592 (2008).
36. Michael, R. et al. Hyperspectral Raman imaging of neuritic plaques and neurofibrillary tangles in brain tissue from Alzheimer's disease patients. *Sci. Rep.* **7**, 15603 (2017).
37. Flynn, J. D., Jiang, Z., & Lee, J.C. Segmental ¹³C-labeling and Raman microspectroscopy of α -synuclein amyloid formation. *Angew. Chem. Int. Ed.* **57**, 17069-17072 (2018).
38. Xue, C., Lin, T.Y., Chang, D. & Guo, Z. Thioflavin T as an amyloid dye: fibril quantification, optimal concentration and effect on aggregation. *R. Soc. Open Sci.* **4**: 160696 (2017).
39. Hong, G. et al. Through-skull fluorescence imaging of the brain in a new near-infrared window. *Nat. Photon.* **8**, 723-730 (2014).
40. Hilderbrand, S.A. & Weissleder, R. Near-infrared fluorescence: application to in vivo molecular imaging. *Curr. Opin. Chem. Biol.* **14**, 71-79 (2010).
41. Bouteiller, C., et al. Novel Water-Soluble Near-Infrared Cyanine Dyes: Synthesis, Spectral Properties, and Use in the Preparation of Internally Quenched Fluorescent Probes. *Bioconjugate Chem.* **18**, 1303-1317 (2007).

42. Koenig, A., et al. In vivo mice lung tumor follow-up with fluorescence diffuse optical tomography. *J. Biomed. Opt.* **13**, 011008 (2008).
43. Koenig, A., et al. Fluorescence diffuse optical tomography for free-space and multifluorophore studies. *J. Biomed. Opt.* **15**, 016016 (2010).
44. Josserand, V., et al. Electrochemotherapy guided by intraoperative fluorescence imaging for the treatment of inoperable peritoneal micro-metastases. *J. Control. Release.* **233**, 81-87 (2016).
45. Saar, B. G. et al. Video-rate molecular imaging in vivo with stimulated Raman scattering. *Science* **330**, 1368-1370 (2010).
46. Camp, C. H. et al. High-Speed Coherent Raman Fingerprint Imaging of Biological Tissues. *Nat. photon.* **8**, 627-634 (2014).
47. Hanzcyc, P., Samoc, M. & Norden, B. Multiphoton absorption in amyloid protein fibres. *Nat. Photon.* **7**, 969-972 (2013).
48. Tao, K., Makam, P., Aizen, R. & Gazit E. Self-assembling peptide semiconductors. *Science* **358**, eaam9756 (2017).
49. Berger, O. et al. Light-emitting self-assembled peptide nucleic acids exhibit both stacking interactions and Watson-Crick pairing. *Nat. Nanotech.* **10**, 353-360 (2015).
50. Plissonneau, M., Pansieri, J. et al. Gd-nanoparticles functionalization with specific peptides for β -amyloid plaques targeting. *J. nanobiotechnool.* **14**, 60 (2016).
51. Pansieri, J., Halim, M.A. et al. Mass and charge distributions of amyloid fibers involved in neurodegenerative diseases: mapping heterogeneity and polymorphism. *Chem. Sci.* **9**, 2791-2796 (2018).
52. Sulatskaya, A.I., Rodina, N.P., Povarova, O.I., Kuznetsova, I.M. & Turoverov, K.K. Different conditions of fibrillogenesis cause polymorphism of lysozyme amyloid fibers. *J. Mol. Struct.* **1140**, 52-58 (2017).
53. Kavanagh, G. M., Clark, A. H., & Ross-Murphy, S. B. Heat-induced gelation of globular proteins: part 3. Molecular studies on low pH β -lactoglobulin gels. *Internat. J. Biol. Macromol.* **8**, 41-50 (2000).
54. Lembré, P., Di Martino, P. & Vendrely, C. Amyloid peptides derived from CsgA and FapC modify the viscoelastic properties of biofilm model matrices. *Biofouling* **30**, 415-426 (2014).

Acknowledgments

This work was supported by Euronanomed ENMII JTC2012 (project 2011-ERA-002-01- Dia-Amyl) and the French National Research Agency (ANR) through the grants ANR-12-RPIB Multimage and ANR-17-CE09-0013 Bionics (ANR-17-CE09-0013-01 & ANR-17-CE09-0013-02). J. Pansieri is grateful to the Fondation pour la Recherche Médicale (FRM) for the granting of his PhD fellowship (grant #: FRM DBS2013112844<0). A. Rongier and S.-J Lee acknowledge Commissariat à l’Energie Atomique et aux Energies Alternatives (CEA) for the funding of their respective CEA-Phare PhD fellowships. We warmly thank M. Dumoulin (University of Liège, Liège, Belgium) for the generous gift of α -synuclein, and S. Denti and S. Chierici (UMR5250-DCM (CNRS/Univ. Grenoble Alpes), Grenoble, France) for the generous gift of hTau used in this work. This research benefited from resources of the European Synchrotron Radiation Facility (ESRF, Grenoble, France). In particular we acknowledge M. Burghammer, M. Sztucki and T.G. Dane of the Microfocus beamline ID13. We thank D. Fenel, C. Moriscot & G. Schoehn from the Electron Microscopy platform of the Integrated Structural Biology of Grenoble (ISBG, UMI3265). We extend our thank to L. Gonon and V. Mareau (UMR5819-SyMMES (CEA/CNRS/Univ. Grenoble Alpes), Grenoble, France) for helpful discussions on Raman scattering. Authors are grateful to L. Kurzawa, (μ Life platform of CEA-Grenoble/BIG and UMR5168-LPCV (CEA/CNRS/Univ. Grenoble Alpes), Grenoble, France) for helpful discussions and specific advices on confocal microscopy. Fluorescence imaging systems used in this study were acquired thanks to France Life Imaging (French program “Investissement d’Avenir” grant; “Infrastructure d’avenir en Biologie Sante”, ANR-11-INBS-44 0006). This work was also supported by NeuroCoG IDEX UGA in the framework of the “Investissements d’avenir” program (ANR-15-IDEX-02).

Author contributions

J.P. and V.F. conceived and designed the work, and wrote most of the text of this paper. J.P., S.-J. L., D.I., O.C. and C.V. realized the *in vitro* characterizations of the amyloid fibres; A.R., T.D. and P.R. conceived, performed and analysed the X-ray scattering experiments; M.M.S. and E.K. collected and prepared the human samples; J.P. and C.M. designed and performed the *ex-vivo* experiments; V.J., M.G., J.V., A.F., Y.U. and J.L.G. performed the 3D and 2D fluorescence imaging and analysed the data. J.P., C.M. and V.F. coordinated all experiments and compiled the results. J.P. C.M., P.R., V.F. contributed ideas and interpretation and edited the text. All co-authors discussed and commented on the manuscript.

Competing financial interests

The authors declare no competing financial interests.

Additional information

Supplementary section 1
Supplementary Fig. 1 to 14
Movies M1 to M4

Legends:

Table 1: Change of luminescence properties of 13 amyloid proteins before and after fibre formation. The enhancement of peptides CSNNFGA and NNLAITVA is unknown, due

to the lack of lag phase and fast aggregation into fibres. (See “methods” for the formation of the various amyloid fibres).

Figure 1. (a&c) Luminescence of dispersions of Het-s prion domain (a) and A β ₁₋₄₂ (c) amyloid fibres in buffers. Excitation wavelength: 340 nm (pink), 360 nm (blue), 380 nm (cyan) and 440 nm (green), and from 600 to 670 nm (red colour scale). A multiplying factor (either x25 or x30) has been applied to NIR spectra in order to show both types of luminescence on the same graph. **(inset)** TEM images of Het-s prion domain the scale bar is worth 100 nm. **(b&d) Fluorescence microscopy:** transmission mode **(bottom right)** and fluorescence microscopy images with emission in the UV-Vis ($\lambda_{exc.} = 390 \pm 10$ nm, $\lambda_{em.} = 460 \pm 50$ nm) **(top left)**, green ($\lambda_{exc.} = 475 \pm 10$ nm, $\lambda_{em.} = 530 \pm 50$ nm) **(top right)**, and NIR ($\lambda_{exc.} = 620 \pm 60$ nm, $\lambda_{em.} = 700 \pm 75$ nm, false red colour) **(bottom left)**. **(b) Aligned Het-s prion domain amyloid fibres:** The scale bars worth 100 μ m. **(d) Brain slices of AD mice in cortex area:** Scale bars correspond to 50 μ m. Amyloid deposits are visible without extrinsic fluorophores (arrows).

Figure 2. Luminescence properties of insulin amyloid protein during fibre growth process: **(a) blue luminescence of insulin amyloid fibres:** Emission spectra of fibres (continuous lines): $\lambda_{exc.}$: 340 nm (pink), 360 nm (blue), 380 nm (cyan) and 440 nm (green)) and monomers (dashed lines: same colours); excitation spectra of insulin amyloid fibres (dash-dot-dash lines): $\lambda_{em.}$: 430 nm (pink), 444 nm (blue) and 458 nm (cyan); **(inset)** TEM images insulin of amyloid fibres, the scale bar is worth 100 nm; **(b) NIR luminescence of insulin amyloid fibres: emission spectra of fibres** (continuous lines of red scale colours): $\lambda_{exc.}$: from 600 nm to 670 nm and monomers (dashed lines: same colours); excitation spectra of insulin amyloid fibres (dash-dot-dash lines: the emission wavelengths correspond to the maximum emission wavelength). **(c) Kinetics of formation of amyloid fibres of insulin** simultaneously monitored through the blue luminescence (blue triangles: $\lambda_{exc.}$: 360 nm) and the NIR signal (dark red circles: $\lambda_{exc.}$: 640 nm).

Figure 3. (a&b) Confocal microscopy images of amyloid deposits *ex vivo* on brain slices of Alzheimer’s patients within the hippocampus area. 3D modelling of the two amyloid deposits from 60 sections recorded through blue emission ($\lambda_{exc.}$: 350-420 nm, $\lambda_{em.}$: 440-500 nm) images. 3D modelling Images were analysed with Vaa3D software. **(insets)** Typical sections of the reconstructed amyloid deposits monitored in the blue range. Scale bars correspond to 5 μ m.

Figure 4. Detection of amyloid deposits by 3D NIR imaging in AD and control mice. **(a&b, top panels)** fDOT imaging on live animals ($\lambda_{exc.}$: 690 nm (laser light) and $\lambda_{em.}$: 730 \pm 30 nm). **(a&b, bottom panels)** Fresh brain sections in the cortex area were observed with the MacroFluo set up with a 515-560 nm excitation and a 590 nm long pass emission filter. **(c)** Higher NIR signal intensities were observed in the brain volume of AD mice in comparison to control mice as measured in 11 mice/group. **(d)** Age distribution of both populations.

Figure 5. Non-invasive detection of amyloid deposits by 2D NIR imaging using Fluobeam[®]800. **(a&b)** 2D imaging of the anesthetized mice was performed *in vivo* directly on the head of the animals **(top panels)** and *ex vivo* on the corresponding brains after sacrifice and extraction from the skull **(bottom panels)**. Two representative mice from the AD and control groups are presented. **(c)** Mapping of the NIR signal intensity distribution within a 3D

graph. **(d)** The mean of local standard deviation (MLSD) as well as the mean of gradient (MG) were calculated (see experimental section) for each animal (AD, n= 11 and WT, n= 11) *in vivo* (**top panels**) and *ex vivo* (**bottom panels**). **(e)** *Ex vivo* values of MLSD and MG vs *in vivo* values of AD animals (red spots) and control mice (blue spots).

Polypeptide	Trp/Tyr/Phe	Extinction coef. (M ⁻¹ .cm ⁻¹)	Blue luminescence enhancement	NIR Stokes shift (nm) (exc. : 640 nm)
Disease related:				
Aβ ₁₋₄₂	0/1/3		x3	56
<i>htau</i>	0/1/1		x6	53
α-synuclein	0/4/2		x3.5	58
TTR (V30M)	2/5/4		x3	55
IAPP	0/1/2		x3	55
Model proteins:				
Het-s prion domain	1/1/1		x8	60
β-lactoglobulin	2/4/3	~ 450 (340 nm)	x3.5	62
α-lactalbumin	4/4/4		x1	52
HSA	3/21/30		x1	56
lysozyme	6/3/3	~ 300 (360 nm)	x4	63
insulin	0/4/3		x36	56
Peptides:				
CSNNFGA	0/0/1	~ 400 (330 nm)	?	55
NNLAIVTA	0/0/0		?	58

Table 1: Change of luminescence properties of 13 amyloid proteins before and after fibre formation. The enhancement of peptides CSNNFGA and>NNLAIVTA is unknown, due to the lack of lag phase and fast aggregation into fibres. (See “methods” for the formation of the various amyloid fibres).

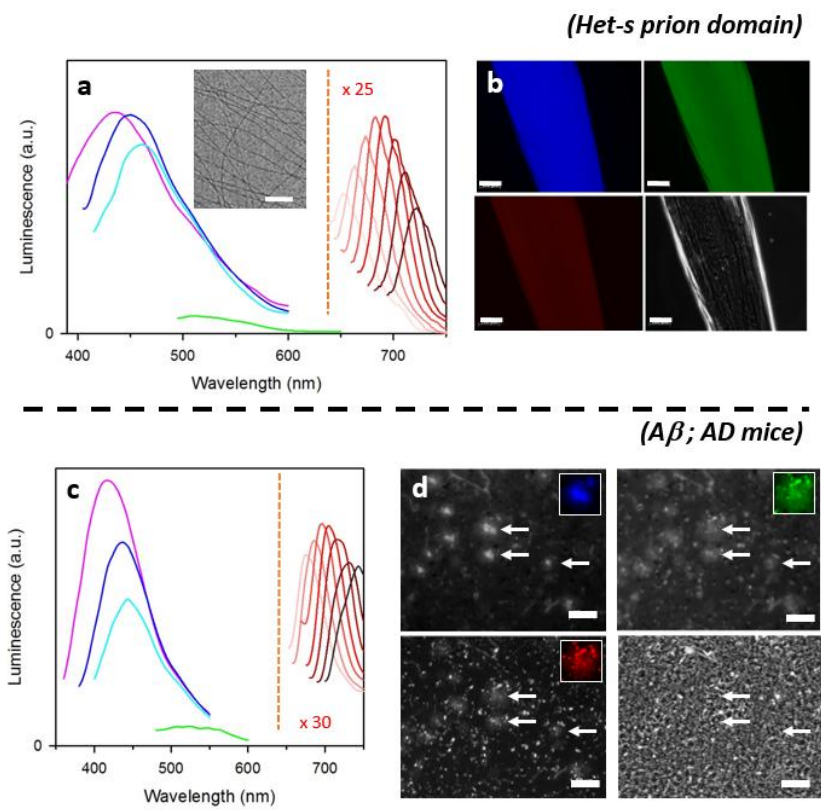


Figure 1

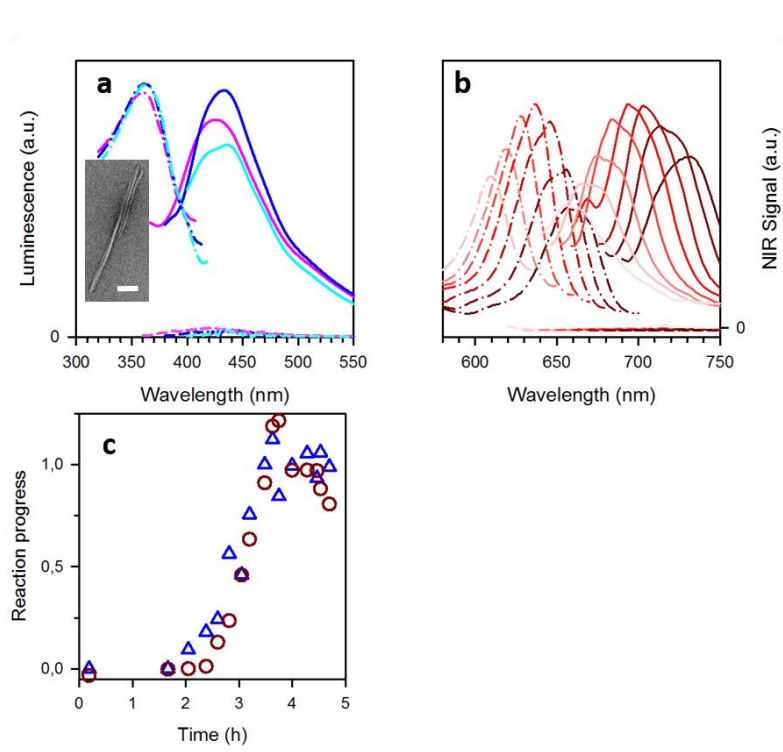


Figure 2

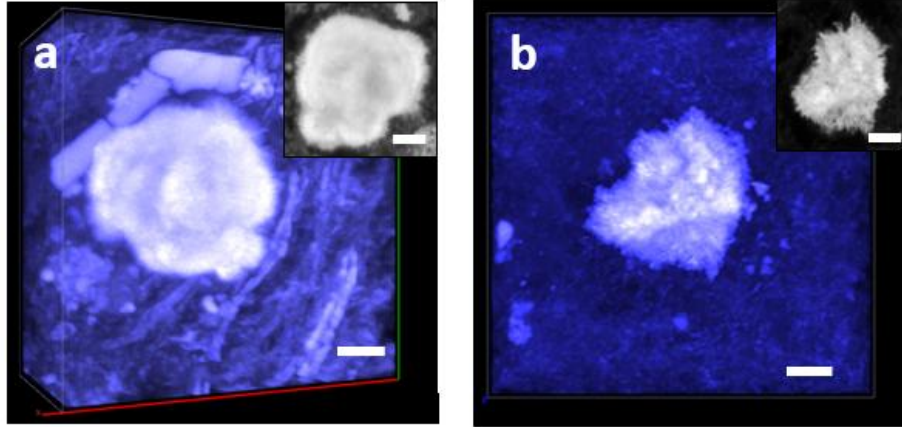


Figure 3

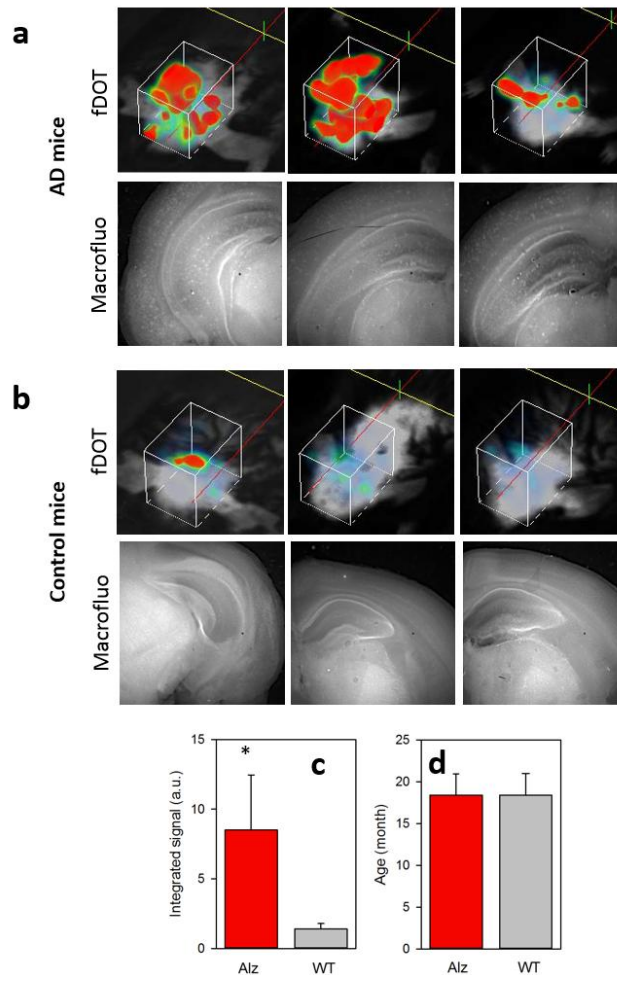


Figure 4

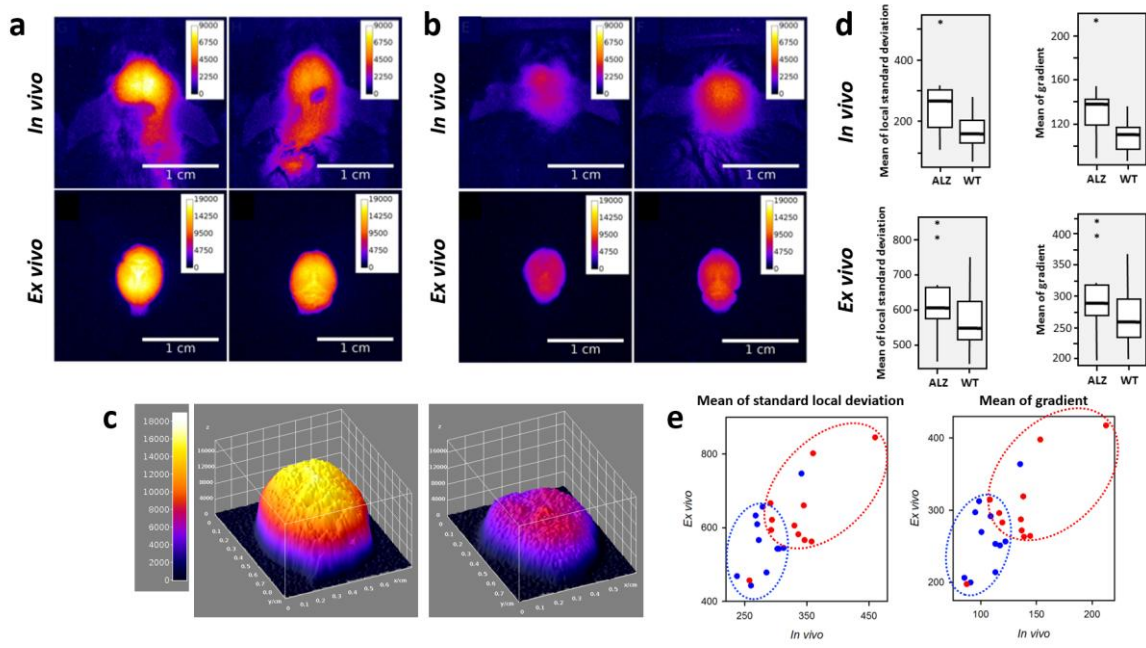


Figure 5